European Cells and Materials Vol. 46 2023 (pages 119-137) DOI: 10.22203/eCM.v046a06 ISSN 1473-2262

CHANGES IN OSTEOGENESIS BY HUMAN DENTAL PULP STEM CELLS ON PORCINE DECELLULARISED ADIPOSE TISSUE SOLID FOAMS OF DIFFERENT POROSITY

Jon Luzuriaga[1,2], Nerea García-Urkia[3], Jone Salvador-Moya[1], Beatriz Pardo-Rodríguez[1], Iker Etxebarria[1], Francisco-Javier Fernandez-San-Argimiro[3], Beatriz Olalde[3], Fernando Unda[1], Jose Ramon Pineda[1,4], Iratxe Madarieta[3,*] and Gaskon Ibarretxe[1]

[1] Department of Cell Biology and Histology, Faculty of Medicine and Nursing, University of the Basque Country, UPV/EHU, Leioa, 48940, Bizkaia, Spain
[2] Department of Physiology, Faculty of Medicine and Nursing, University of the Basque Country, UPV/EHU, Leioa, 48940, Bizkaia, Spain
[3] TECNALIA, Basque Research and Technology Alliance (BRTA), E20009 Donostia-San Sebastian, Spain
[4] Achucarro Basque Center for Neuroscience Fundazioa, Leioa, 48940, Bizkaia, Spain

Abstract

The extracellular matrix of white adipose tissue (AT) is a very promising biomaterial for tissue engineering, due to its abundance, easy accessibility, malleability, and proven biological activity. Decellularised AT (DAT) can be processed by freeze-drying in acetic acid solutions, and changing the DAT concentration in the solution gives rise to three-dimensional (3D) scaffolds of different stiffness and porosity. In a previous report, we demonstrated that human Dental Pulp Stem Cells (hDPSCs) could differentiate to osteoblasts and generate mineralised bone on 3D solid foams of porcine Decellularised Adipose Tissue (pDAT) at a concentration of 0.5 % (w/v). In this research work, we assessed whether and how osteogenesis by hDPSCs would be regulated by testing pDAT solid foams formulated at three different concentrations: 0.25 % (w/v), 0.5 % (w/v), and 1 % (w/v), which showed different stiffness, porosity and water retention properties. As a control condition we tested solid foams formulated with 0.5 % bovine Collagen-I. Thus, we performed Alkaline Phosphatase and Alizarin Red staining, together with Transmission Electron Microscopy and the detection of osteoblastic differentiation markers Osterix and Osteocalcin at both protein and transcript level, to compare the osteogenesis mediated by hDPSCs grown on all these 3D scaffolds, in the presence or absence of osteoblastic induction media. Our results demonstrate that pDAT at 0.25 % supported osteogenesis better than the rest of tested scaffolds, including bovine Collagen-I, in 3D hDPSC cultures. This enhanced osteogenesis could be attributed to the formulation of 0.25 % pDAT solid foams, which presented a higher porosity.

Keywords: Dental pulp stem cells, 3D culture, adipose tissue, osteogenesis, extracellular matrix, decellularisation, solid foam, cell differentiation, mineralisation.

***Address for correspondence:** Iratxe Madarieta, TECNALIA, Basque Research and Technology Alliance (BRTA), E20009 Donostia-San Sebastian, Spain
Telephone number: +34 667 11 63 72 (IM) Email: iratxe.madarieta@tecnalia.com
ORCID: 0000-0002-1097-9326 (IM)

List of Abbreviations

AT	Adipose tissue
DAT	Decellularised Adipose Tissue
3D	Three-dimensional
hDPSCs	Human Dental Pulp Stem Cells
pDAT	Porcine Decellularised Adipose Tissue
bCOL-I	Bovine Collagen I
PBS	Phosphate buffered saline
SEM	Scanning Electron Microscopy
IUPAC	International Union of Pure and Applied Chemistry
BJH	Barrett–Joyner–Halenda
BET	Brunauer–Emmett–Teller
PFA	Paraformaldehyde
AR	Alizarin Red
ECM	Extracellular matrix
MSCs	Mesenchymal Stem Cells

Introduction

Three dimensional (3D) human stem cell culture systems relying on biologic scaffold materials constitute an effective strategy to generate humanised tissues with very important applications in drug screening and tissue bioengineering. Accordingly, the interactions that take place between stem and progenitor cells and their surrounding extracellular matrix (ECM), critically affect their differentiation outcome to adult cell lineages (Nowwarote *et al.*, 2022; Rao *et al.*, 2022). Understanding how physical and biochemical cues from the ECM affect stem cell lineage commitment and differentiation is thus of paramount importance to tissue bioengineering.

In the particular case of bone tissue, the stiffness and porosity of the ECM scaffold are regarded as two of the main factors that regulate differentiation of multipotent Mesenchymal Stem Cells (MSCs) to bone producing osteoblastic cells (Steward and Kelly, 2015; Xu *et al.*, 2017). Thus, there is ample evidence demonstrating that osteogenic differentiation of MSCs is promoted by growing these cells on stiff substrates above 25-40 KPa (El-Rashidy *et al.*, 2021; Engler *et al.*, 2006; Lee *et al.*, 2014a; Lee *et al.*, 2014b), whereas it is reduced by growing them on soft substrates below 1 KPa (Engler *et al.*, 2006; Lee *et al.*, 2014b).

Regarding the effect of ECM porosity on osteogenesis, scaffolds with a higher degree of porosity have been shown to support bone formation better than less porous ones (Gupte *et al.*, 2018; Jodati *et al.*, 2020; Krieghoff *et al.*, 2019). Accordingly, macropore sizes above 300 μm were considered as optimal to facilitate angiogenesis and promote deposition of calcified bone ECM by MSCs or osteoblast cells seeded on different types of biomaterials (Haugen *et al.*, 2019; Karageorgiou and Kaplan, 2005; Murphy *et al.*, 2010). However, other studies have reported that smaller macropores of up to 50 μm may also sustain osteogenesis to a similar extent (Itälä *et al.*, 2001). So, the optimal ECM pore size for osteogenesis may be context-dependent, and not only their size but other factors like how these matrix pores are interconnected may play a pivotal role as well. The produced bone matrix, once mature and fully calcified, may also hamper nutrient and gas exchange. This "barrier effect" could also compromise the metabolic balance of the seeded cells in MSC 3D cultures once the process of osteogenesis and matrix mineralisation has been engaged (Salgado *et al.*, 2004).

Human Dental Pulp Stem Cells (hDPSCs) may be regarded as some of the most promising stem cell types for cell therapy, because of their extremely high versatility for multilineage differentiation, including the possibility to give rise to many different types of mature adult cells like osteoblasts, adipocytes, chondrocytes, muscle cells, vascular cells and even neural cells (Aurrekoetxea *et al.*, 2015; Luzuriaga *et al.*, 2021). These stem cells also possess additional advantages that make them a very attractive option for cellular therapy in human subjects, such as their easiness of extraction in aseptic conditions, their immunomodulatory properties, high metabolic adaptability, and good chances of implementation into autologous transplant

therapy (Ibarretxe *et al.*, 2012; Luzuriaga *et al.*, 2021; Tirino *et al.*, 2011).

In particular, the osteo/odontogenic differentiation potential of hDPSCs is especially powerful, compared to other types of osteogenic human MSCs (Alksne *et al.*, 2022; Huang *et al.*, 2009; Kotova *et al.*, 2021; Ma *et al.*, 2019; Pisciotta *et al.*, 2012). Thus, hDPSCs may readily differentiate to osteoblast/odontoblast lineage cells in standard foetal serum containing cell culture media, and similarly to other MSCs, this process can also be significantly accelerated by the addition of several soluble differentiation inducing factors like dexamethasone, beta-glycerol phosphate, and ascorbate (Aurrekoetxea *et al.*, 2015; Langenbach and Handschel, 2013). Therefore, hDPSCs are a particularly well suited stem cell type for bone tissue engineering.

In this research work we cultured hDPSCs on porcine Decellularised Adipose Tissue (pDAT) solid foams, obtained with different concentration. pDAT constitutes a very interesting biomaterial for tissue engineering applications, due to is complete biodegradability, biological activity, and low immunogenicity (Cicuéndez *et al.*, 2021; Yang *et al.*, 2020). In a previous report, we demonstrated that pDAT solid foams were optimal scaffolds for osteogenesis, with performance levels comparable to the gold standard bovine Collagen I (bCOL-I) (Luzuriaga *et al.*, 2022). However, the hDPSC-mediated osteogenesis on pDAT solid foams could be further enhanced by optimising their structural properties such as stiffness and porosity. pDAT solid foams are relatively soft scaffolds with a stiffness usually lower than 1 KPa (Garcia-Urkia *et al.*, 2022; Luzuriaga *et al.*, 2022). However, both the stiffness and the porosity of the solid foams can be finely tuned by changing the pDAT concentration in the solution during their preparation. Thus, in this work we tested pDAT solid foams generated from solutions at 0.25 %, 0.5 %, and 1 % concentration (w/v), to search for the conditions that best supported osteogenic differentiation and matrix mineralisation by hDPSCs in 3D culture.

Materials and Methods

Adipose tissue decellularisation and processing as solid foams

The methodology of adipose tissue (AT) decellularisation and processing has been thoroughly described elsewhere (Madarieta *et al.*, 2017; Madarieta *et al.*, 2023). Briefly, Porcine AT was cleaned, creamed with a beater, and homogenised on ice using a Polytron (PT3100; Kinematica AG, Malters, Switzerland) with two different rods (PT-DA3012/EC and PT-DA-12/2EC-F154) at 12,000 rpm for 5 min. The homogenised tissue (25 mL) was centrifuged at 900 g for 5 min with 25 mL of ultrapure water to produce the phase separation of lipids, which were discarded, and protein pellets were taken and treated with isopropanol (ref. 59307, Gibco-BRL, Paisley, UK) overnight under orbital shaking at room temperature. The protein-containing phase was then cleaned with phosphate buffered saline (PBS) supplemented with an antibiotic-antimycotic solution (1 %, ref. 15240062, Gibco, Waltham, MA, USA) and protease inhibitors (ref. 539128, Merck Life Science SL, Spain) and treated with 1 % (v/v) Triton x-100 and 0.1 % (v/v) ammonium hydroxide (ref. 221228, Merck Life Science SL, Spain) for 36 h in an orbital shaker at room temperature. Then, the pDAT material was cleaned and lyophilised. Finally, the material was milled using a mixer mill (Restch MM400, Hann, Germany) to generate a fine-grainy powder (Fig. 1**a**) which could be kept at 4 °C in a vacuum desiccator until use. Milled pDAT met the decellularisation criteria as previously described (Cicuéndez *et al.*, 2021; Madarieta *et al.*, 2017; Madarieta *et al.*, 2023).

Different solid foams were prepared by the freeze-drying method all the while maintaining the freezing temperature at – 20 °C. Thus, 0.25 % (w/v), 0.5 % (w/v) and 1 % (w/v) milled pDAT, or alternatively 0.5 % (w/v) bovine collagen I (bCOL-I; ref C9879, Sigma, St. Louis, MO, USA) were added to a 0.5 M acetic acid solution and homogenised by magnetic stirring for 48 h. After that, different moulds were used to prepare the solid foams. For Scanning Electron Microscopy (SEM) and mechanical and swelling testing, 20 mm in diameter and 3 mm thickness Teflon moulds were used with a 1 mL solution. For *in vitro* cell culture assays, pDAT

and collagen solutions were cast into conventional 48- and 24-well polystyrene tissue culture treated plates (approximately 200 μL/cm^2). All the solid foams were obtained by freezing the solutions in the molds at – 20 °C overnight, and then freeze-drying them (0.63 mbar and – 20 °C) for 72 h. Freeze-dried solid foams were sterilised using ethylene oxide (Esterilizacion SL, Barcelona, Spain) for 270 min at 38 °C and 40 % relative humidity and kept at 4 °C in a vacuum desiccator until use.

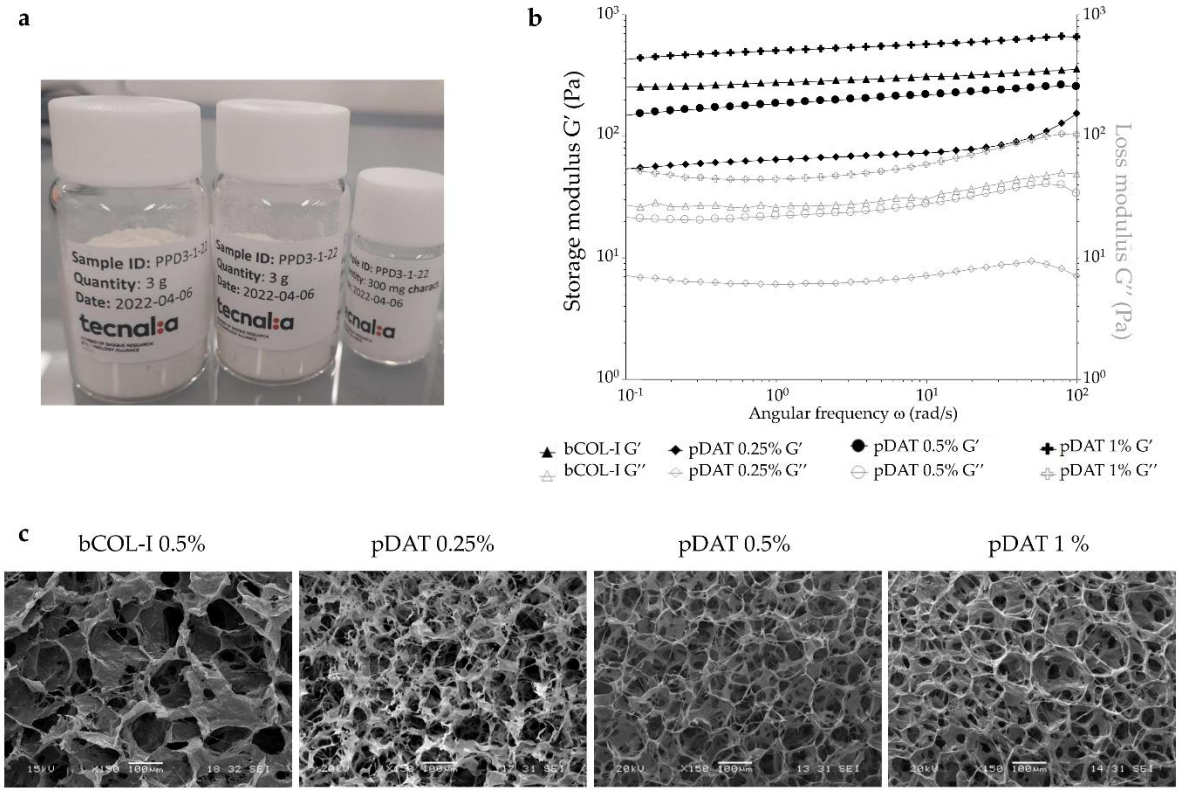

Fig. 1. Viscoelastic behaviour and ultrastructual morphology of the 3D solid foams. (**a**) pDAT powder of different concentration obtained after decellularisation. (**b**) Logarithmic quantification of the viscoelastic behaviour showing storage and loss modulus. (**c**) Ultrastructural images of the different solid foams. Scale bars = 100 nm.

Assessment of swelling and mechanical properties of solid foams

Mechanical properties of the pDAT and collagen solid foams were assessed by oscillatory shear rheology, with parallel-plate geometry (20-mm diameter steel with a gap of 1 mm) on a TA instruments HR20 rheometer (Waters, New Castle, DE, USA), as previously described (Garcia-Urkia *et al.*, 2022; Luzuriaga *et al.*, 2022). Stress amplitude sweeps were performed at a constant frequency of 0.1 Hz to establish the amplitude parameter for each sample and to ensure that all data were collected in a linear viscoelastic regime. All the measurements were made in constant deformation control mode over a frequency range from 0.01 to 10 Hz.

Swelling properties of the solid foams were determined by a water absorption assay. The dry weight (Wd) was recorded from lyophilized foams prior to bringing them to maximum hydration in distilled water for 24 h. Thereafter, the foams were carefully blotted to remove the excess liquid and the wet weight (Ws) was recorded. The equilibrium water content (% ECW) and mass swelling ratio (S) were calculated as previously described (Garcia-Urkia *et al.*, 2022; Luzuriaga *et al.*, 2022).

Assessment of porosity of solid foams

The International Union of Pure and Applied Chemistry (IUPAC) defined three classes of porous materials (Sing, 1985), namely

microporous (pore size < 2 nm), mesoporous (> 2 nm and < 50 nm) and macroporous (> 50 nm). The presence of macropores was analysed using Scanning Electron Microscopy (SEM) images of solid foams by Fiji-ImageJ free software (v1.54f. National Institute of Health, Bethesda, Maryland, USA). A total of 3 images and a 0.8 mm^2 surface area per image were analysed, counting only the pores that were completely visible in the image and taking their widest diameter. Results are shown as number of pores per image and diameter. The presence of micro and mesopores was assessed by using Barrett–Joyner–Halenda (BJH) analysis based on capillary condensation (Barrett *et al.*, 1951). About 35 replicas of each sample type were individually incorporated into the flask of the gas porosimeter measurement system (Accelerated Surface Area and Porosimetry System, ASAP2420, Micromeritics, Norcross, GA, USA) and liquid N_2 at 77K was applied as a gas, the pressure was measured at each moment of the analysis, and the amount of gas absorbed was determined. The porosity was quantified by the Brunauer–Emmett–Teller (BET) model to determine the total area (Surface area, g/cm^3). The Density Functional Theory (DFT) was used as the model to determine the distribution of the porosity. The pore volume (cm^3/g) was calculated by extrapolating the values of each point of the isotherm.

3D culture of hDPSCs on solid foams

Primary cultures of hDPSCs from third molar teeth were established following a well-established protocol, as thoroughly described elsewhere (Gronthos *et al.*, 2002; Pineda *et al.*, 2022; Uribe-Etxebarria *et al.*, 2017). The hDPSCs were cultured in standard Dulbecco's modified Eagle's medium (DMEM) supplemented with 10 % fetal bovine serum (FBS), L-glutamine (1 mM, ref. G7513, Sigma, St. Louis, MO, United States) and the antibiotics penicillin (100 U/mL) and streptomycin (150 μg/mL) (Ref.15140-122, Gibco, Waltham, MA, USA). After the first culture passage (P1), cells were transferred to 3D culture plates where the bottom of the wells was filled with a layer of solid foams of 0.25 %, 0.5 % or 1 % (w/v) pDAT, or control 0.5 % (w/v) bCOL-I. 3D cultures of hDPSCs on solid foams were kept for a period of 2 to 4 weeks to carry out the different experiments. Briefly, hDPSCs were cultured on solid foams in standard medium or alternatively with osteogenic medium supplemented with osteodifferentiation factors, as previously described (Luzuriaga *et al.*, 2022). The osteogenic differentiation medium consisted of regular culture medium supplemented with 50 μM ascorbic acid (ref. A4403; Sigma, MO, USA), 20 mM β-glycerolphosphate (ref. 50020; Sigma, MO, USA) and 10 nM dexamethasone (ref. D4902; Sigma, MO, USA).

Histochemical and immunohistochemical assessment of osteogenic differentiation and solid foam mineralisation

These protocols have been thoroughly described elsewhere (Madarieta *et al.*, 2023). The *in situ* differentiation of hDPSCs to osteoblastic cells on solid foams was assessed by Alkaline Phosphatase (ALP) staining and immunohistochemistry (IHC) against BGLAP/osteocalcin after 2 weeks in culture. For ALP staining, solid foams were fixed for 1 min with 4 % paraformaldehyde (PFA) and then washed with 0.05 % Tween-20 in PBS buffer. ALP staining was performed in Tris-HCl buffer at pH = 9.5, using 5-Bromo-4-chloro-3-indolyl phosphate/Nitro Blue tetrazolium (ref. B3804; Sigma, MO, USA) as substrate. The staining progress was checked every 3 min, and the reaction was stopped by washing foams with PBS three times for 5 min. Then, ALP absorbance was measured at 420 nm using a Synergy HT Multi-Mode Microplate Reader (Biotek, Winooski, VT, USA). For the acquisition of microscopy images, solid foams were counterstained with 4',6-diamino-2-phenilindol (DAPI, 1:1000; Invitrogen, Camarillo, CA, USA), and then detached from the culture plates to be mounted onto conventional glass slides. Images of mounted foams were taken with an epifluorescence and transmitted light OLYMPUS IX71 microscope, coupled to an OLYMPUS DP71 digital camera (Olympus Iberia, L'Hospitalet de Llobregat, Barcelona, Spain).

For IHC experiments, pDAT and bCOL-I solid foams were fixed with 4 % PFA, and the blocking performed with 10 % goat serum (ref. 50197Z; Invitrogen, CA, USA) both for 10 min at room temperature. Then, samples were incubated with anti-Osteocalcin/BGLAP (1:200,

ref. ab93876, Abcam, Cambridge, UK) at 4 °C overnight, and the staining was revealed by incubation with fluorescent secondary antibody Alexa fluor 488 (1:200, ref. A32731, ThermoFisher Scientific, Waltham, MA, USA) for 1 h at room temperature. Cell nuclei were counterstained with DAPI (1:1000; Invitrogen, CA, USA), and detached from the culture plates to be mounted onto glass microscopy slides. Samples were observed with a confocal microscope Zeiss LSM800 (Zeiss, Overkochen, Germany) coupled to an Axiocam 305 (Zeiss, Overkochen, Germany) color camera. Relative BGLAP immunostaining was calculated by dividing the overall IF labelling intensity by the number of nuclei present in the confocal orthogonal image projection, using Fiji-Image J free software.

Mineralisation/calcification of solid foams was assessed by Alizarin Red (AR) staining. hDPSCs cultured for 4 weeks in pDAT or bCOL-I solid foams were fixed with 4 % PFA for 10 min. Samples were then washed with distilled water and stained using 2 % AR (Acros organics, Sigma, MO, USA) at pH 4.1-4.3 for 45 min on the dark at room temperature. The staining solution was removed and samples were washed with distilled water until no AR could be found dissolved on water. AR absorbance was measured at 405 nm using a Synergy HT Multi-Mode Microplate Reader (Biotek, Winooski, VT, USA). Thereafter, foams were detached from culture plates and mounted onto microscopy slides to obtain higher resolution images. Cell nuclei were counterstained with DAPI (1:1000; Invitrogen, CA, USA). Images of mounted foams were taken with an epifluorescence and transmitted light OLYMPUS IX71 microscope, coupled to an OLYMPUS DP71 digital camera.

Scanning and Transmission Electron Microscopy (SEM; TEM)

The microarchitecture and porosity of solid foams was assessed by SEM. Samples were mounted, and pulse coated with gold and visualised with a JEOL JSM-5910 LV SEM (JEOL, Tokyo, Japan) with an accelerating voltage of 10 kV. The cell and matrix ultrastructure in solid foams were assessed by TEM at 4 weeks after hDPSC seeding. Foams were fixed with 2 % glutaraldehyde (ref. G6257, Sigma, MO, USA) and embedded in Epon Polarbed resin (Electron Microscopy Sciences, Hatfield, PA, USA). Ultrathin sections (70 nm) were deposited onto 150 mesh copper grids (ref: G2150C 150 Square Mesh copper 3.05 mm, AGAR Scientific, Essex, UK), post-stained with 2 % uranyl acetate and 0.2 % lead citrate in distilled water (refs AGR1260A and AGR1210 respectively, AGAR Scientific, Essex, UK), and finally visualized in a Philips EM208S transmission electron microscope (Eindhoven, North Bravant, The Netherlands). Digital images were acquired with an integrated Jeol JEM 1400 Plus camera (Akishima, Tokyo, Japan).

RNA extraction, reverse transcription and quantitative real-time (RT-qPCR)

Differentiation of hDPSCs to osteoblastic cells was also assessed at transcript level, as previously described (Luzuriaga *et al*., 2022). RNA was extracted by a 4:1 solution of Trizol (ref 10296010, Invitrogen, Waltham, USA) and chloroform (ref C0549-1PT, Sigma, MO, USA). Samples were then centrifuged at 12,000 g and 4 °C to separate organic and aqueous phases. The latter were collected and RNA precipitation was made by incubating for 10 min with isopropanol at 1:1 ratio. Then, samples were centrifuged again at 12,000 g for 5 min at 4 °C, to form a gel-like pellet containing the RNA, which was washed with 75 % ethanol, dried, and finally resuspended in 20 µL of elution buffer (ref 12183020, RNA mini-kit, Invitrogen, Waltham, USA). RNA purity and concentration were calculated by measuring the 260/280 nm absorbance ratio, using a Synergy HT spectrophotometer (Biotek, Winooski, VT, USA). Reverse transcription was made using using the iScript cDNA kit (Ref.1708890; BioRad, Hercules, CA, USA). Finally, qPCR experiments were conducted using an iCycler My iQ™ Single-Color Real-Time PCR Detection System (BioRad, Hercules, CA, USA), using 4.5 µL of Power SYBR® Green PCR Master Mix 2× (ref 4367659, Applied Biosystems™, Waktham, MA, USA), 0.5 µL of primers (0.3125 µmol/L), 0.3 µL of cDNA (1.5 ng/µL) and nuclease-free water for a total volume reaction of 10 µL. Data were processed by CFX Manager™ Software (BioRad, Hercules, CA, USA). All RT-qPCR reactions yielded only one amplicon as assessed by the melting curve

method. *BGLAP* and *OSTERIX* were taken as representative gene markers of ongoing and terminal osteoblastic differentiation respectively, and their expression was normalised to the average of three housekeeping genes *GAPDH*, *β-ACTIN*, and *RPS18*. The sequences of primers are listed in Table 1.

Table 1. List of primers. (F) forward; (R): reverse; (bp): base pairs.

Primers	Sequence 5′-3′	Annealing (°C)	Amplicon (bp)
β-ACTIN (F)	GTTGTCGACGACGAGCG	58.5	93
β-ACTIN (R)	GCACAGAGCCTCGCCTT	59.7	93
GAPDH (F)	CTTTTGCGTCGCCAG	60.3	131
GAPDH (R)	TTGATGGCAACAATATCCAC	60.8	131
RPS18 (F)	CAGAAGGATGTAAAGGATGG	53.0	200
RPS18 (R)	TATTTCTTCTTGGACACACC	52.9	200
BGLAP (F)	CTCACACTCCTCGCCCTATT	58.88	143
BGLAP (R)	CGCCTGGGTCTCTTCACTAC	59.83	143
OSTERIX (F)	TGAGGAGGAAGTTCACTATG	53.79	200
OSTERIX (R)	CATTAGTGCTTGTAAAGGGG	53.96	200

Statistical analyses

Data were analysed using SPSS v.28 (IBM, Endicott, NY, USA) and Excel software. Data sets were first subjected to a Saphiro-Wilk test to verify that they fitted to normality criteria before comparisons between sample groups. Statistical differences between sample conditions were then assessed by ANOVA followed by Bonferroni post-hoc test. Confidence intervals were set at 95 % ($p < 0.05$), 99 % ($p < 0.01$) and 99.9 % ($p < 0.001$).

Results

Characterisation of solid foams made with different pDAT concentrations

The AT decellularisation procedure was carried out as previously described (Cicuéndez *et al.*, 2021; Luzuriaga *et al.*, 2022). Once the fine-grainy powder of pDAT was obtained (Fig. 1**a**), this was reconstituted at different concentrations (0.25 %, 0.5 %, and 1 % w/v) in acetic acid solution to obtain 3D solid foams with different porosity and stiffness after freeze-drying. These ECM biomaterials were incorporated to conventional polystyrene cell culture plates for hDPSC culture. The viscoelastic behaviour of the solid foams showed higher G′ (storage modulus) values than G′′ (loss modulus) during the entire range of frequencies, indicating the predominance of the elastic behaviour over the viscous one for all assayed samples. The solid foams showed higher average storage modules (G′) according to the increase of pDAT concentration in the formulation: 68.7 ± 10.6 Pa, 176.4 ± 26.4 Pa and 633.8 ± 75.7 Pa for pDAT 0.25 %, 0.5 % and 1 % respectively. Thus, there was approximately an order of magnitude of stiffness difference (G′and G′′) between the pDAT foams at the upper and lower concentration ends of 0.25 % pDAT, and 1 % pDAT. 0.5 % bCOL-I solid foams used as control scaffold showed a higher storage and viscous modulus than its counterpart pDAT at 0.5 % (Fig. 1**b**, Table 2). These results are in agreement with water absorption and microstructural analysis of the solid foams, because the water contribution to the overall resistance of the materials to deformation was higher in pDAT solid foams at 0.5% than in bCOL-I at the same concentration.

The microstructural SEM analysis of the solid foams showed that they all presented homogeneous porous structures, with substantial differences in shape and number. 0.25 % pDAT solid foams showed more irregular pores. 1 % pDAT and 0.5 % bCOL-I solid foams showed much better defined pores with lower connectivity. 0.5 % pDAT foams showed well defined and interconnected pores (Fig. 1**c**).

Overall, the highest levels of porosity were found on pDAT 0.25 % solid foams, which showed a much higher density of macropores, particularly of those with ≤ 50 μm diameter (Fig. 2**a**). In this regard, all pDAT solid foams were found to be far more porous than bCOL-I ones, where the presence of macropores on pDAT 0.5 % and pDAT 1 % foams approximately doubled that of bCOL-I foams (Fig. 2**a**). pDAT 0.25 % was the most porous solid foam, with a total density of macropores that almost doubled that of the other two pDAT foams (Fig. 2**b**). BET analysis also showed the presence of mesopores within the solid foams, with an average pore size in the range of 44 to 53 Å (Table 3). The total area and volume of mesopores was higher in pDAT 0.5 % and bCOL-I 0.5 %, especially compared to pDAT 1 %, which was the least porous material on this respect. pDAT 0.25 % solid foams showed intermediate mesopore levels (Table 3). No micropores were detected in any of the assayed samples (not shown).

Table 2. Properties of pDAT-based solid foams.

ID	Material (mg/mL)	Water absorption		Average modulus	
		(EWC, %)	S ratio	G′ (Pa)	G″ (Pa)
pDAT (0.25 %)	2.5	98.6 ± 0.0	69.2 ± 0.7	68.7 ± 10.6	6.9 ± 1.0
pDAT (0.5 %)	5	99.4 ± 0.0	165.6 ± 6.3	176.4 ± 26.4	21.9 ± 4.3
pDAT (1 %)	10	98.4 ± 0.2	50.2 ± 4.5	633.8 ± 75.7	66.1 ± 16.8
bCOL-I (0.5 %)	5	99.0 ± 0.0	99.3 ± 1.8	289.0 ± 26.6	29.5 ± 3.1

Table 3. BET analysis of mesoporosity of solid foams.

	pDAT 0.25 %	pDAT 0.5 %	pDAT 1 %	bCOL-I 0.5 %
BET surface area (m^2/g)	37.41	52.6	20.67	53.41
Total area in pores (m^2/g)	14.554	23.67	9.45	26.18
Total volume in pores (cm^3/g)	0.04	0.06	0.02	0.06
Average pore diameter (Å)	44.91	52.8	53.52	47.08

hDPSCs grown on 3D pDAT solid foams generated osteoblastic cells with different efficiency depending on pDAT concentration, with highest rates at 0.25 % pDAT

We sought to address whether changes in pDAT solid foam stiffness would reflect in changes of hDPSC differentiation efficiency to osteoblastic cells, by IHC and RT-qPCR analysis. The immunolabeling of the bone matrix protein BGLAP was found to be much higher in 0.25 % pDAT foams, than in 1 % pDAT foams (316 ± 61 % vs 68 ± 10 % respectively, with respect to 100 ± 30 % of bCOL-I; Fig. 3**a,b**; $p < 0.01$). BGLAP is a bone matrix protein whose expression is indicative of an osteoblastic cell commitment but does not necessarily imply a terminally concluded osteoblastic differentiation (El-Rashidy *et al.*, 2021; Irastorza *et al.*, 2019). The transcription factor OSTERIX (SP7) was thus chosen as an alternative gene marker more specific of terminally differentiated osteoblastic cells (Liu *et al.*, 2020). Immunolabeling against OSTERIX was also found to be much higher in the 0.25 % pDAT foams (202.91 ± 12 % vs 100 ± 6 % of bCOL-I). This difference was even larger when DPSCs were cultured under osteodifferentiation induction conditions (Fig. 4**a-c**). Interestingly, a decreasing intensity of BGLAP and OSTERIX immunofluoresence in 3D hDPSC cultures was observed as the pDAT concentration increased, with lowest staining levels for 1 % pDAT, intermediate levels for 0.5 % pDAT, and highest levels for 0.25 % pDAT (Fig. 3**a,b** and Fig. 4**a,b**). This pattern was also maintained at transcript level, where qPCR data showed a much larger BGLAP and OSTERIX expression in the 0.25 % pDAT matrix condition, with respect to 0.5 % pDAT and 1 % pDAT solid foams (Fig. 4**d**; $p < 0.001$).

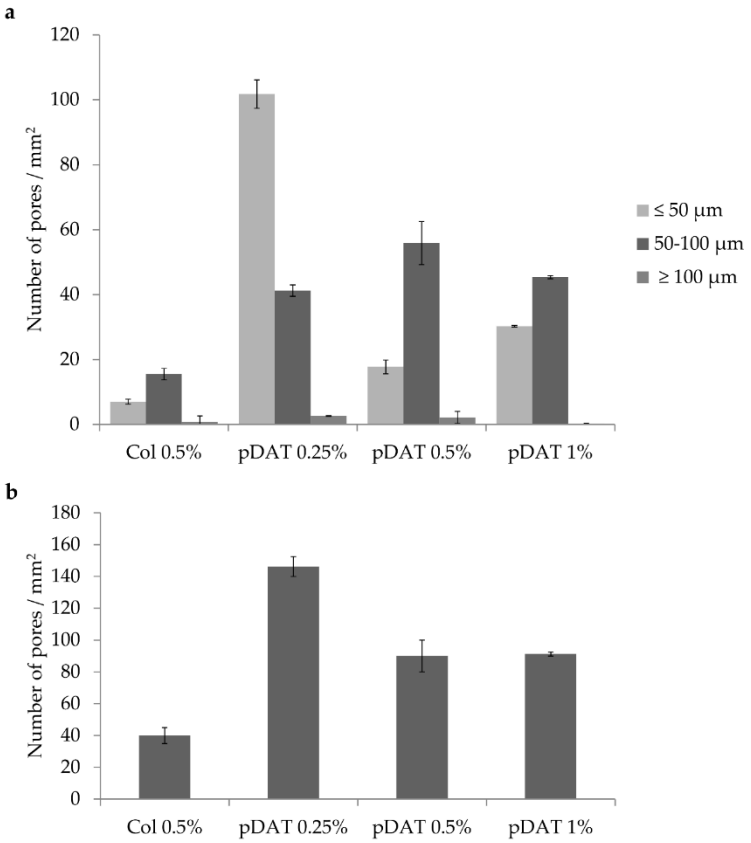

Fig. 2. Relative density and sizes of macropores in solid foams. (**a**) SEM images of the different solid foams were analysed and macropores were classified according to their diameter. (**b**) Quantification of relative macropore density as total number of macropores per SEM image area. Data shown as mean ± SD.

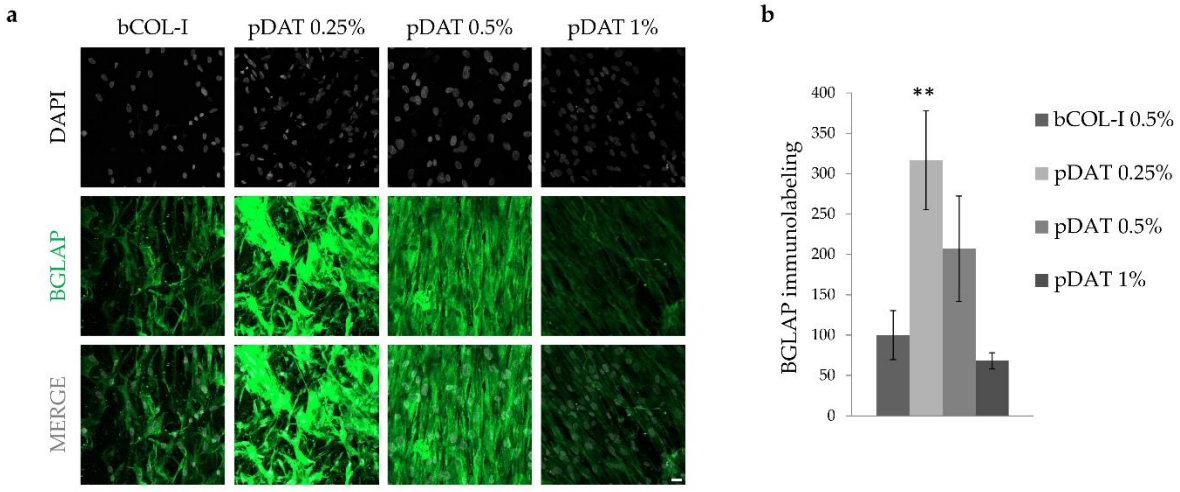

Fig. 3. BGLAP immunolabeling of hDPSCs seeded on pDAT and b-COL I solid foams after 2 weeks. (**a**) BGLAP immunostaining images of 3D cultures after 14 days in osteodifferentiation conditions. Scale bar = 20 µm. (**b**) Quantification of BGLAP bone matrix protein immunostaining. Data shown as mean ± SEM. **: $p < 0.01$ (n = 4).

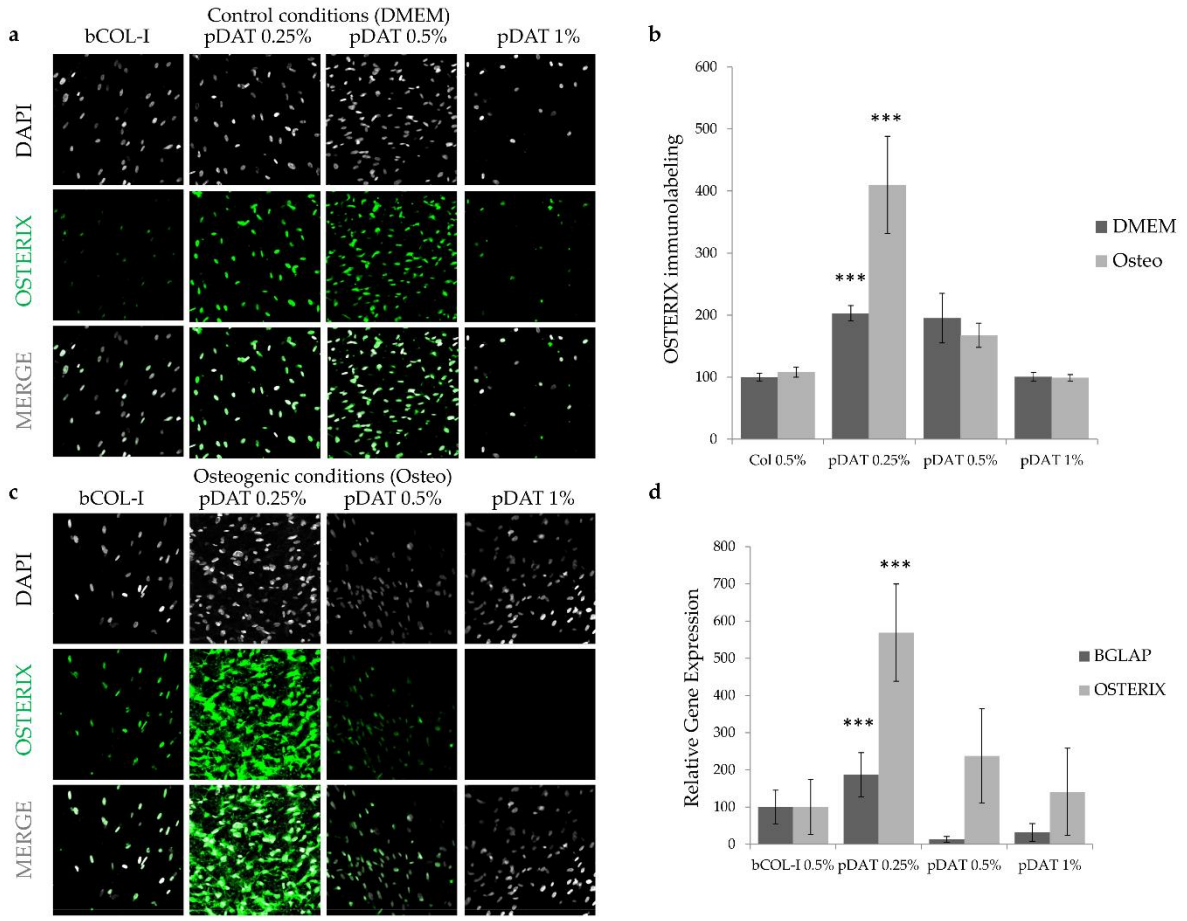

Fig. 4. OSTERIX and BGLAP expression by hDPSCs seeded on pDAT and b-COL I solid foams after 2 weeks. (**a,c**) OSTERIX immunostaining images of 3D cultures in control **(DMEM; a)** and osteodifferentiation **(Osteo; c)** conditions. Scale bar = 20 μm. (**b**) Quantification of OSTERIX immunostaining. Data shown as mean ± SEM. ***: $p < 0.001$ (n = 4). (**d**) Relative differences in gene transcript expression for BGLAP and OSTERIX osteoblastic differentiation markers. Data shown as mean ± SEM. ***: $p < 0.001$ (n = 6).

hDPSCs grown on 0.25 % pDAT mineralised the solid foam matrix with greater efficiency than on 0.5 % pDAT, 1 % pDAT, and 0.5 % bCOL-I

Immunostaining and RT-PCR experiments suggested a more efficient osteoblastic differentiation on 0.25 % solid foams, compared to the rest of conditions. Thus, it could be expected that this enhanced differentiation would also translate into differences at histochemical level (i.e., enhanced matrix mineralisation). Two types of histochemical labelling were performed: ALP staining, and Alizarin Red staining. ALP histochemistry at 2 weeks post-seeding showed higher labelling levels when hDPSCs were grown on 0.25 % pDAT solid foams, in the presence of osteoblastic induction media (Fig. 5**a-c**). This was despite a high background absorbance by solid foams at 420 nm, which partly overshadowed the specific ALP signal (not shown). The final proof of matrix mineralisation is the presence of hydroxyapatite mineral in the solid foams, which can be stained with AR, but hydroxiapatite crystal accumulation and matrix mineralisation is a relatively slow process which can only be assessed in the long-term. Thus, we performed AR staining to solid foams at 4 weeks after hDPSC seeding and 3D culture in both control and osteoinductive conditions (Fig. 6). Again, we found some background absorbance in the solid foams, which was higher in 1 % pDAT and 0.5 % b-COL I foams, intermediate in 0.5 % pDAT foams, and lower in the case of 0.25 % pDAT foams (Fig. 6**c**). We did not find any differences in AR staining on hDPSC-containing solid foams in control conditions (Fig. 6**a-c**). However, a very intense AR staining was found

in solid foams containing hDPSCs grown under osteoinductive conditions, which was clearly distinguishable from the background absorbance (Fig. 6**b,c**). Measuring AR absorbance levels on the foams cultured in osteoinductive media showed statistically significant differences, with 0.25 % pDAT solid foams displaying significantly higher mineralisation levels than the other three conditions (Fig. 6**b-d**; $p < 0.01$). Once again a decreasing gradation of AR absorbance was found to be in accordance with the pDAT concentration on the solid foams, with highest staining levels found at 0.25 % pDAT (168 ± 19 %; $p < 0.01$), and lowest levels at 1 % pDAT (102 ± 8 %). Control solid foams of 0.5 % bCOL-I showed mineralisation levels (100 ± 18 %) which were smaller than those of 0.25 % pDAT, but not significantly different from those of 0.5 % pDAT and 1 % pDAT (Fig. 6**b-d**).

To assess in detail the cellular phenotypes and the calcified matrix ultrastructure in the 3D solid foam scaffolds, we performed a TEM analysis. Thus, we found that mineralised matrix regions could be distinguished from the rest of non-mineralised regions in the solid foam by their higher electron density (Fig. 7 and Fig. 8**a**). We found out that many of the seeded cells in the foams had effectively differentiated to osteoblastic cells, which were actively secreting highly intertwined collagen fibers that underwent a rapid calcification, as assessed by TEM (Fig. 7). In contrast, some other collagen containing regions that were initially part of the solid foams remained non-calcified (Fig. 8**a**). Consistently with the rest of the assays, the *de novo* produced electrodense calcified matrix regions were far more abundant in pDAT 0.25 % solid foams than in the rest of conditions (Fig. 7). The cross-section diameter of these newly synthesised collagen fibrils was about 50-100 nm, and was much smaller than those present on bovine collagen solid foams (bCOL-I). The cell morphology of *in situ* osteodifferentiated DPSCs included a well-developed endoplasmic reticulum consistent with a high protein secretion activity, also showing fine cellular processes which were getting progressively embedded in the electrodense calcified collagen matrix (Fig. 7; dashed yellow line).

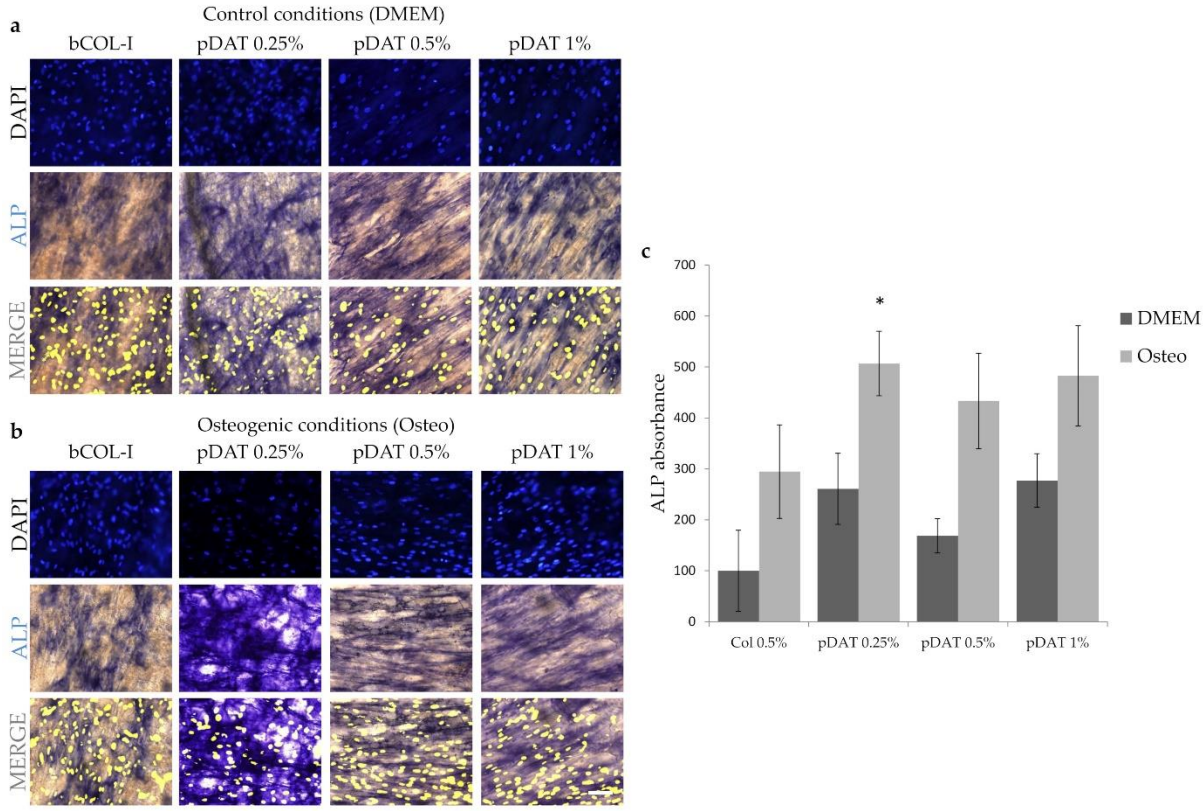

Fig. 5. ALP staining of hDPSCs seeded on 3D pDAT and b-COL I solid foams after 2 weeks. (**a**) Control conditions. (**b**) Osteodifferentiation conditions. Brightfield images were taken with the same light intensity on the different solid foams. Cell nuclei are counterstained with DAPI. Scale bar (**a,b**) =

50 μm. (**c**) Quantification of ALP absorbance by plate photometry in different foams after background subtraction. Data shown as mean ± SEM. *: $p < 0.05$ (n = 7-9).

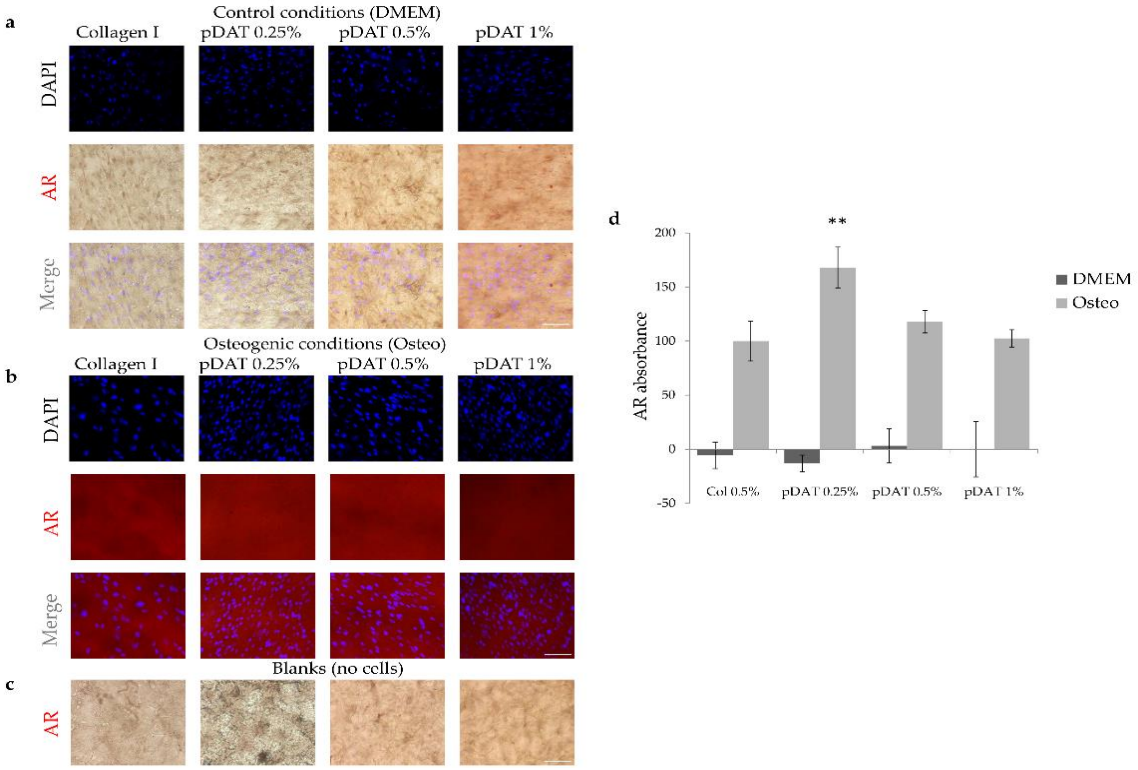

Fig. 6. AR staining of hDPSCs seeded on pDAT and b-COL I solid foams after 4 weeks. (**a**) Control conditions. (**b**) Osteodifferentiation conditions. Brightfield images were taken with the same light intensity for each of the different solid foams. Cell nuclei are counterstained with DAPI. Scale bar (**a,b**) = 50 μm. (**c**) Brightfield images showing background absorbance of solid foams with no seeded cells. (**d**) Quantification of AR absorbance by plate photometry in different foams after background subtraction. Data shown as mean ± SEM. **: $p < 0.01$ (n = 4).

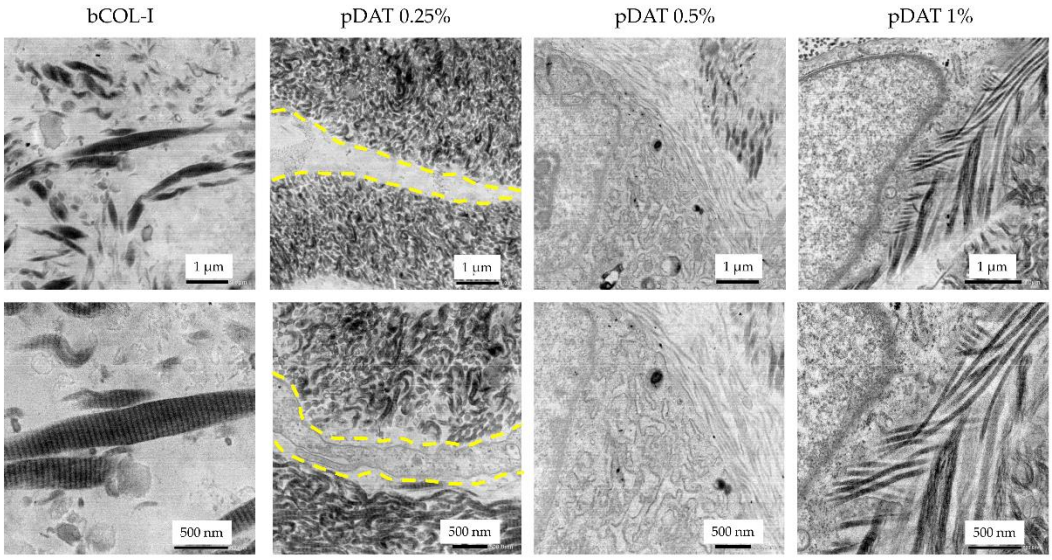

Fig. 7. TEM images of hDPSCs-seeded solid foams after 4 weeks, showing osteoblastic cell phenotypes and matrix mineralisation. Top panel: Lower magnification; Bottom panel: higher magnification. Newly secreted collagen fibers calcify and form compact electrodense bundles. Secretory cells with a prominent Rough Endoplasmic Reticulum were detected (showed for 0.5 % pDAT). The pDAT solid foam scaffold at 0.25 % underwent a more efficient mineralization, featured

by a more abundant presence of electrodense fiber bundles, and fine cellular processes getting embebbed on the electrodense calcified bone matrix (dashed yellow line). Note the bigger diameter of control bovine collagen fibers (bCOL-I; left panel), compared to de novo secreted human collagen bundles by osteoblast-differentiated cells in 0.25 % pDAT and 1 % pDAT. Scale bars: 1 μm (top), 500 nm (bottom).

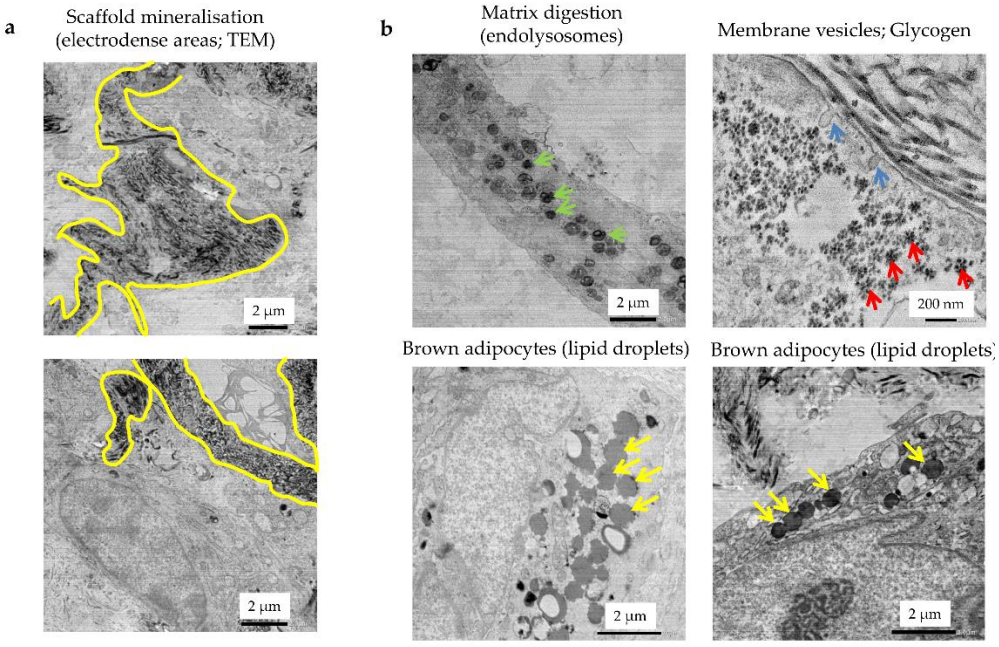

Fig. 8. TEM images of hDPSCs-seeded solid foams after 4 weeks, showing ECM calcification, ECM degrading cells, and multilocular adipocytes. (**a**) Sharp transitions in calcification of solid foam areas featuring de novo secreted electrodense collagen fibers by osteoblast differentiated hDPSCs on 0.25 % pDAT solid foams. Limits of highly calcified foam areas are marked by a yellow line. (**b**) The seeded hDPSCs digest and remodeled the solid foams, as assessed by the presence of endolysosomes (b; top left; 0.5 % pDAT, green arrows), and endocytic vesicles (b; top right; 1 % pDAT, blue arrows). Some cells showed abundant glycogen granules (b; top right; 1 % pDAT, red arrows). Some cells also underwent a brown multilocular adipocyte-like differentiation, as assessed by the presence of numerous lipid droplets together with mitochondria in the cell cytoplasm. Lipid droplets showed a characteristic spherical and homogeneous appearance that distinguished them from the rest of cell organelles (b; bottom panels; 0.25 % and 0.5 % pDAT, yellow arrows). Scale bars: 2 μm for all images, except top right (200 nm).

Cell phenotypes in 3D solid foams after 4 weeks of DPSC-seeding include osteoblastic cells, ECM degrading cells, and multilocular adipocytes

In addition to cellular morphologies characteristic of secretory osteoblasts, we also identified cells displaying variable amounts of endolysosomes, which suggested an ECM digestion activity (Fig. 8**b**, green arrows). Thus, it appeared that the seeded hDPSCs were undertaking a true ECM remodelling within the solid foam, secreting new ECM, but also degrading some of it. Consistent with this interpretation, both exocytic and endocytic vesicles could be observed in the plasma membrane of some of the seeded cells (Fig. 8**b**, blue arrows). Some cells were also identified as storing large amounts of glycogen granules (Fig. 8**b**, red arrows). Finally, some of the seeded hDPSCs also showed a characteristic multilocular adipogenic differentiation phenotype after 4 weeks, which could be recognised by the formation of numerous cytosolic lipid droplets of homogeneous content, with moderate to high electron density (Fig. 8**b**, yellow arrows). These brown fat-like cell morphologies could be observed in all solid foams except bCOL-I, with no apparent

distinction according to the different pDAT concentrations.

Discussion

Decellularised ECM biomaterials obtained from adipose tissue constitute very promising tissue engineering scaffolds for 3D cell culture and personalised regenerative therapies (Badylak, 2007; Yang *et al.*, 2020). In a previous report, we found that solid foams derived from pDAT could support osteogenesis after hDPSC seeding, to similar effectiveness to the so far widely employed gold standard bCOL-I (Luzuriaga *et al.*, 2022; Rico-Llanos *et al.*, 2021). However, pDAT solid foams can be tailored according to a variety of factors. An obvious one is the pDAT concentration in the starting freeze-dried solution, which would affect both the stiffness and porosity of the resulting scaffold. In this study, we generated solid foams of different pDAT concentrations, which resulted in scaffolds with different stiffness and water retention properties. Our initial assumption was that the stiffer (i.e., more concentrated) pDAT solid foams obtained at 1 % might have been better scaffolds to support hDPSC osteodifferentiation and osteogenesis. It had been already amply reported that the osteogenic differentiation efficiency of MSCs depended on the substrate characteristics, with stiffer surfaces promoting osteogenic differentiation, and softer substrates promoting adipogenic and/or neural differentiation (Engler *et al.*, 2006; Lee *et al.*, 2014a). However, even though significant differences were present between conditions, increasing the pDAT concentration from 0.25 % to 1 % did not increase the stiffness of the solid foams above 1KPa (Fig. 1), which meant that even in the most concentrated condition (1 % pDAT), the stiffness of our pDAT biomaterial would still be comparatively very low, with respect to previous studies where an enhanced osteodifferentation was observed at stiffness levels ranging over 25-30 KPa (Engler *et al.*, 2006; Lee *et al.*, 2014b).

Besides stiffness, ECM porosity is regarded as another fundamental factor governing osteogenesis (Gupte *et al.*, 2018; Jodati *et al.*, 2020; Krieghoff *et al.*, 2019). It was proposed that pore diameters of at least 100 μm and optimally 300-400 μm were necessary to allow an adequate cell infiltration, metabolic exchange, and angiogenesis, to support bone matrix formation (Haugen *et al.*, 2019; Hulbert *et al.*, 1970; Murphy *et al.*, 2010). Nevertheless, other reports have come to challenge that idea, suggesting that smaller pore sizes up to 50 μm may be effective in promoting osteogenesis as well (Bobyn *et al.*, 1980; Itälä *et al.*, 2001). Apart from the mere pore size, the level of interconnectivity of those pores also matters, and so does the presence of micro and mesopores which could facilitate gas and nutrient exchange to the matrix-infiltrating cells.

In our system of osteogenesis in relatively soft 3D solid foams of pDAT and bCOL-I, we found that porosity was a crucial characteristic of the scaffold that supported its mineralisation by hDPSCs. We found that the most effective solid foam to support hDPSCs osteogenesis was the 0.25 % pDAT, which was shown to be largely more porous, particularly to what concerned the presence of macropores in a size range around 50 μm, as assessed by SEM (Fig. 1**c** and Fig. 2**a**). It should be emphasised that throughout this work we have followed the porosity classification by IUPAC (Sing, 1985), which is not universally adopted (Jodati *et al.*, 2020). The greater porosity of pDAT 0.25 % solid foams correlated well with an enhanced osteogenesis of hDPSCs in these conditions, which was corroborated by different techniques including: IHC, RT-PCR, ALP, AR, and TEM, assessing not only osteoblastic differentiation, but also the biomaterial mineralisation. We thus attribute the better ability of 0.25 % pDAT solid foams to support osteogenesis to a higher material porosity. It is to be remarked that the principal difference of 0.25 % pDAT to the rest of solid foams is the much greater abundance of small macropores up to 50 μm. No increases in pore density were observed regarding big macropores > 50 μm, where 0.5 % pDAT and 1 % pDAT foams showed higher relative values. As for the presence of mesopores between 2 nm and 50 nm, the least porous material was 1 % pDAT, and the most porous was 0.5 % bCOL-I (Table 3).

Therefore, we found a clear correlation between solid foam porosity and osteogenesis in our 3D hDPSC cultures. 0.25 % pDAT solid foams have the highest density of macropores, which explains the better results obtained in the mineralisation and osteoblastic detection assays, compared to the rest of formulations.

Comparing bCOL-I and pDAT at the same concentration of 0.5 %, it was found that pDAT had a higher macroporosity than bCOL-I, which could explain the better performance of the former in some of the assays. As for 1 % pDAT, this was the material that showed the lowest mesoporosity, and arguably the worst osteogenic capability, even though that was not significantly different from that of bCOL-I. Thus, in our 3D culture system in the absence of microfluidic perfusion, pores of different sizes may all play an important role in supporting osteogenesis. As assessed by confocal microscopy, in our 3D culture conditions, most cells apparently preferred not to migrate very deep inside the solid foams and stayed within the first 200-400 μm below the foam surface. To allow a deeper cell penetration in the absence of an *in vivo* vasculature, the solid foam would have needed some sort of nutrient and/or gas exchange system, which is especially important in the case of bone tissue engineering, due to the additional substance diffusion restrictions imposed by the presence of a calcified ECM (Salgado *et al*., 2004). Thus, according to this view, the more porous microstructure of 0.25 % pDAT solid foams would provide for a better and more efficient metabolic exchange, which would allow for a higher rate of bone matrix deposition than in the rest of conditions.

The pDAT ECM-derived biomaterial is deemed to be non-immunogenic due to its extensive processing and effective decellularisation (Cicuéndez *et al*., 2021; Yang *et al*., 2020). Compared to other osteo-permissive biomaterials like bCOL-I, the procurement of pDAT can be much cheaper and easier (Luzuriaga *et al*., 2022; Madarieta *et al*., 2023). Our group has developed and patented both solvent-related and enzyme-related methodologies for pDAT extraction, and each can be adapted to the application of choice (Brown *et al*., 2011; Cicuéndez *et al*., 2021). More compatibility experiments will still be necessary to assess the translatability of pDAT to regenerative therapies in human patients, but the experiences with other biological products of porcine origin have been so far substantially positive (Badylak, 2004; Mosala Nezhad *et al*., 2016; Rana *et al*., 2017). Moreover, pDAT showed a remarkable capacity for processing, and can be used to obtain a large variety of scaffolds, including hydrogels for cell encapsulation and injection, and bio-inks for 3D bioprinting (Dzobo *et al*., 2019; Kabirian and Mozafari, 2020; Zhang *et al*., 2017), allowing an extraordinary versatility for tissue engineering.

Apart from xenogenic sources, our group is also investigating on human derived DAT (hDAT) from liposuction surgery in collaboration with hospitals, thus allowing a fully personalised clinical application of this biomaterial, whether for the design of *in vitro* screening platforms including autologous 3D cell cultures, or *in vivo* grafts for tissue regeneration. In a previous study, we found that hDAT was much more refractory to mineralisation by hDPSCs, likely owing to the higher human specificity of the different biomodulatory signals naturally present in the adipose tissue ECM (Luzuriaga *et al*., 2022). However, this resistance to osteogenesis can also be beneficial in some circumstances, such as the reconstruction of bone-adjacent soft tissues like tendons and ligaments (Ibarretxe, 2022; Screen *et al*., 2015). Even though pDAT had rather different bioinductive characteristics to hDAT, we found that a proportion of the seeded hDPSCs still differentiated to adipocyte cells in the presence of pDAT (Fig. 8**b**). The adipogenic phenotype of these cells was multilocular, corresponding to brown fat-like adipocytes. This brown-fat bioinduction is also of interest from the point of view of regenerative therapies of joints or ligaments, which can benefit from a locally increased thermogenesis in the grafted area, to accelerate endogenous healing mechanisms (Diaz *et al*., 2014). Finally, it could be very interesting to combine these pDAT and hDAT scaffolds with hDPSCs grown in vasculogenic serum-free media, as recently described (Luzuriaga *et al*., 2019; Luzuriaga *et al*., 2020; Mattei *et al*., 2021). The development of autologous micro-tissues harbouring endogenous vasculature could constitute a real leap forward in the development of more effective regenerative cell therapies, and for all their versatility and fine-tuning possibilities, these decellularised adipose tissue ECM materials appear to be very attractive tools for this purpose.

Conclusions

The fine customisation of pDAT solid foams as a scaffold to support osteogenesis in 3D cell culture can significantly enhance the performance of this biomaterial for bone tissue engineering. We report here that significant changes in hDPSC-mediated osteogenesis take place when culturing these cells in 3D pDAT solid foams of different concentration: 0.25 %, 0.5 %, and 1 % (w/v). These tailored pDAT biomaterials presented different stiffness, porosity and water retention properties. The softest foams of pDAT at 0.25 % were the most effective in driving osteoblastic differentiation of hDPSCs and ECM mineralisation, owing to their much higher porosity. The wide-ranging possibilities of pDAT and hDAT formulations offer very positive prospects for an optimisation of tissue engineering constructs for personalised medicine.

Acknowledgements

Authors appreciate the kind technical assistance of Ricardo Andrade, Irene Fernández, and Alejandro Díez-Torre, staff members of the SGIKER service of Analytical Microscopy of UPV/EHU. Porosity analyses were performed by the Porous Solids Laboratory of the Central Research Support Services (SCAI) of the University of Malaga, Spain.

Author contributions

JL, NGU, IM, GI Design and conception of the analysis; JL, JSM, NGU, BPR, IE, GI, Data collection; FJFSA, JL, NGU, JSM, IE, IM, GI, Data or analysis tools contribution; JL, NGU, BO, IM, GI, Performed the analysis; JL, NGU, JRP, IM, IE, GI, Wrote the paper; JRP, IM and GI, Reviewed and edited the paper. Funding acquisition: JRP, FU, IM and GI. All authors discussed the results and contributed to the final manuscript.

Ethics approval and consent to participate

This work has been approved by the ethics committees CEISH and CEIAB of the University of the Basque Country (UPV/EHU) for laboratory experimentation with biological material from human and animal origin.

Funding

This research was funded by the by the Basque Government (ELKARTEK program PLAKA KK-2019-00093, and Consolidated Research Groups IT1751-22) and the MCIN/AEI/10.13039/501100011033 -Spanish Ministry of Science and Innovation (PID2019-104766RB-C21).

Conflict of interest

The authors declare no conflict of interest.

References

Alksne M, Kalvaityte M, Simoliunas E, Gendviliene I, Barasa P, Rinkunaite I, Kaupinis A, Seinin D, Rutkunas V, Bukelskiene V (2022) Dental pulp stem cell-derived extracellular matrix: autologous tool boosting bone regeneration. Cytotherapy **24**: 597-607. DOI: 10.1016/j.jcyt.2022.02.002.

Aurrekoetxea M, Garcia-Gallastegui P, Irastorza I, Luzuriaga J, Uribe-Etxebarria V, Unda F, Ibarretxe G (2015) Dental pulp stem cells as a multifaceted tool for bioengineering and the regeneration of craniomaxillofacial tissues. Front Physiol **6**: 289. DOI: 10.3389/fphys.2015.00289.

Badylak SF (2004) Xenogeneic extracellular matrix as a scaffold for tissue reconstruction. Transpl Immunol **12**: 367-377. DOI: 10.1016/j.trim.2003.12.016.

Badylak SF (2007) The extracellular matrix as a biologic scaffold material. Biomaterials **28**: 3587-3593. DOI: 10.1016/j.biomaterials.2007.04.043.

Barrett EP, Joyner LG, Halenda PP (1951) The Determination of Pore Volume and Area Distributions in Porous Substances. I. Computations from Nitrogen Isotherms. J Am Chem Soc **73**: 373-380. DOI: 10.1021/ja01145a126.

Bobyn JD, Pilliar RM, Cameron HU, Weatherly GC (1980) The optimum pore size for the fixation of porous-surfaced metal implants by the ingrowth of bone. Clin Orthop Relat Res: 263-270.

Brown BN, Freund JM, Han L, Rubin JP, Reing JE, Jeffries EM, Wolf MT, Tottey S, Barnes

CA, Ratner BD, Badylak SF (2011) Comparison of three methods for the derivation of a biologic scaffold composed of adipose tissue extracellular matrix. Tissue Eng Part C Methods **17**: 411-421. DOI: 10.1089/ten.TEC.2010.0342.

Cicuéndez M, Casarrubios L, Feito MJ, Madarieta I, Garcia-Urkia N, Murua O, Olalde B, Briz N, Diez-Orejas R, Portolés MT (2021) Effects of Human and Porcine Adipose Extracellular Matrices Decellularized by Enzymatic or Chemical Methods on Macrophage Polarization and Immunocompetence. Int J Mol Sci **22**: 3847. DOI: 10.3390/ijms22083847.

Diaz MB, Herzig S, Vegiopoulos A (2014) Thermogenic adipocytes: From cells to physiology and medicine. Metabolism **63**: 1238-1249. DOI: 10.1016/j.metabol.2014.07.002.

Dzobo K, Motaung KSCM, Adesida A (2019) Recent Trends in Decellularized Extracellular Matrix Bioinks for 3D Printing: An Updated Review. Int J Mol Sci **20**: 4628. DOI: 10.3390/ijms20184628.

El-Rashidy AA, El Moshy S, Radwan IA, Rady D, Abbass MMS, Dörfer CE, Fawzy El-Sayed KM (2021) Effect of Polymeric Matrix Stiffness on Osteogenic Differentiation of Mesenchymal Stem/Progenitor Cells: Concise Review. Polymers **13**: 2950. DOI: 10.3390/polym13172950.

Engler AJ, Sen S, Sweeney HL, Discher DE (2006) Matrix Elasticity Directs Stem Cell Lineage Specification. Cell **126**: 677-689. DOI: 10.1016/j.cell.2006.06.044.

Garcia-Urkia N, Luzuriaga J, Uribe-Etxebarria V, Irastorza I, Fernandez-San-Argimiro FJ, Olalde B, Briz N, Unda F, Ibarretxe G, Madarieta I, Pineda JR (2022) Enhanced Adipogenic Differentiation of Human Dental Pulp Stem Cells in Enzymatically Decellularized Adipose Tissue Solid Foams. Biology **11**: 1099. DOI: 10.3390/biology11081099.

Gronthos S, Brahim J, Li W, Fisher LW, Cherman N, Boyde A, DenBesten P, Robey PG, Shi S (2002) Stem cell properties of human dental pulp stem cells. J Dent Res **81**: 531-535. DOI: 10.1177/154405910208100806.

Gupte MJ, Swanson WB, Hu J, Jin X, Ma H, Zhang Z, Liu Z, Feng K, Feng G, Xiao G, Hatch N, Mishina Y, Ma PX (2018) Pore size directs bone marrow stromal cell fate and tissue regeneration in nanofibrous macroporous scaffolds by mediating vascularization. Acta Biomater **82**: 1-11. DOI: 10.1016/j.actbio.2018.10.016.

Haugen HJ, Lyngstadaas SP, Rossi F, Perale G (2019) Bone grafts: which is the ideal biomaterial? J Clin Periodontol **46**: 92-102. DOI: 10.1111/jcpe.13058.

Huang GT-J, Gronthos S, Shi S (2009) Mesenchymal stem cells derived from dental tissues vs. those from other sources: their biology and role in regenerative medicine. J Dent Res **88**: 792-806. DOI: 10.1177/0022034509340867.

Hulbert SF, Young FA, Mathews RS, Klawitter JJ, Talbert CD, Stelling FH (1970) Potential of ceramic materials as permanently implantable skeletal prostheses. J Biomed Mater Res **4**: 433-456. DOI: 10.1002/jbm.820040309.

Ibarretxe G (2022) Bioactive Materials for Next-Generation Dentistry. Bioengineering **9**: 782. DOI: 10.3390/bioengineering9120782.

Ibarretxe G, Crende O, Aurrekoetxea M, García-Murga V, Etxaniz J, Unda F (2012) Neural crest stem cells from dental tissues: a new hope for dental and neural regeneration. Stem Cells Int **2012**: 103503. DOI: 10.1155/2012/103503.

Irastorza I, Luzuriaga J, Martinez-Conde R, Ibarretxe G, Unda F (2019) Adhesion, integration and osteogenesis of human dental pulp stem cells on biomimetic implant surfaces combined with plasma derived products. Eur Cell Mater **38**: 201-214. DOI: 10.22203/eCM.v038a14.

Itälä AI, Ylänen HO, Ekholm C, Karlsson KH, Aro HT (2001) Pore diameter of more than 100 μm is not requisite for bone ingrowth in rabbits. J Biomed Mater Res **58**: 679-683. DOI: 10.1002/jbm.1069.

Jodati H, Yılmaz B, Evis Z (2020) A review of bioceramic porous scaffolds for hard tissue applications: Effects of structural features. Ceram Int **46**: 15725-15739. DOI: 10.1016/j.ceramint.2020.03.192.

Kabirian F, Mozafari M (2020) Decellularized ECM-derived bioinks: Prospects for the future. Methods **171**: 108-118. DOI: 10.1016/j.ymeth.2019.04.019.

Karageorgiou V, Kaplan D (2005) Porosity of 3D biomaterial scaffolds and osteogenesis. Biomaterials **26**: 5474-5491. DOI: 10.1016/j.biomaterials.2005.02.002.

Kotova AV, Lobov AA, Dombrovskaya JA, Sannikova VY, Ryumina NA, Klausen P,

Shavarda AL, Malashicheva AB, Enukashvily NI (2021) Comparative Analysis of Dental Pulp and Periodontal Stem Cells: Differences in Morphology, Functionality, Osteogenic Differentiation and Proteome. Biomedicines **9**: 1606. DOI: 10.3390/biomedicines9111606.

Krieghoff J, Picke A-K, Salbach-Hirsch J, Rother S, Heinemann C, Bernhardt R, Kascholke C, Möller S, Rauner M, Schnabelrauch M, Hintze V, Scharnweber D, Schulz- Siegmund M, Hacker MC, Hofbauer LC, Hofbauer C (2019) Increased pore size of scaffolds improves coating efficiency with sulfated hyaluronan and mineralization capacity of osteoblasts. Biomater Res **23**: 26. DOI: 10.1186/s40824-019-0172-z.

Langenbach F, Handschel J (2013) Effects of dexamethasone, ascorbic acid and β-glycerophosphate on the osteogenic differentiation of stem cells in vitro. Stem Cell Res Ther **4**: 117. DOI: 10.1186/scrt328.

Lee J, Abdeen AA, Huang TH, Kilian KA (2014a) Controlling cell geometry on substrates of variable stiffness can tune the degree of osteogenesis in human mesenchymal stem cells. J Mech Behav Biomed Mater **38**: 209-218. DOI: 10.1016/j.jmbbm.2014.01.009.

Lee J, Abdeen AA, Kilian KA (2014b) Rewiring mesenchymal stem cell lineage specification by switching the biophysical microenvironment. Sci Rep **4**: 5188. DOI: 10.1038/srep05188.

Liu Q, Li M, Wang S, Xiao Z, Xiong Y, Wang G (2020) Recent Advances of Osterix Transcription Factor in Osteoblast Differentiation and Bone Formation. Front Cell Dev Biol **8**: 601224. DOI: 10.3389/fcell.2020.601224.

Luzuriaga J, García-Gallastegui P, García-Urkia N, Pineda JR, Irastorza I, Fernandez-San-Argimiro F-J, Briz N, Olalde B, Unda F, Madarieta I, Ibarretxe G (2022) Osteogenic differentiation of human dental pulp stem cells in decellularised adipose tissue solid foams. Eur Cell Mater **43**: 112-129. DOI: 10.22203/eCM.v043a10.

Luzuriaga J, Irurzun J, Irastorza I, Unda F, Ibarretxe G, Pineda JR (2020) Vasculogenesis from Human Dental Pulp Stem Cells Grown in Matrigel with Fully Defined Serum-Free Culture Media. Biomedicines **8**: 483. DOI: 10.3390/biomedicines8110483.

Luzuriaga J, Pastor-Alonso O, Encinas JM, Unda F, Ibarretxe G, Pineda JR (2019) Human Dental Pulp Stem Cells Grown in Neurogenic Media Differentiate Into Endothelial Cells and Promote Neovasculogenesis in the Mouse Brain. Front Physiol **10**: 347. DOI: 10.3389/fphys.2019.00347.

Luzuriaga J, Polo Y, Pastor-Alonso O, Pardo-Rodríguez B, Larrañaga A, Unda F, Sarasua J-R, Pineda JR, Ibarretxe G (2021) Advances and Perspectives in Dental Pulp Stem Cell Based Neuroregeneration Therapies. Int J Mol Sci **22**: 3546. DOI: 10.3390/ijms22073546.

Ma L, Hu J, Cao Y, Xie Y, Wang H, Fan Z, Zhang C, Wang J, Wu C-T, Wang S (2019) Maintained Properties of Aged Dental Pulp Stem Cells for Superior Periodontal Tissue Regeneration. Aging Dis **10**: 793-806. DOI: 10.14336/AD.2018.0729.

Madarieta I, Luzuriaga J, Garcia-Gallastegi P, Garcia-Urkia N, Fernandez San- Argimiro FJ, Uribe-Etxebarria V, Jiménez-Rojo L, Unda F, Olalde B, Pineda JR, Ibarretxe G (2023) Decellularized adipose tissue solid foams for hDPSC differentiation to osteogenic and adipogenic cells in 3D culture. Available at: https://www.protocols.io/view/decellularized-adipose-tissue-solid-foams-for-hdps-cqk9vuz6 (Accessed: 01 July 2023).

Madarieta IM, URQUIA NG, GARCÍA RF (2017) Method for producing a decellularized tissue matrix. Available at: https://patents.google.com/patent/WO2017114902A1/en (Accessed: 6 July 2023).

Mattei V, Martellucci S, Pulcini F, Santilli F, Sorice M, Delle Monache S (2021) Regenerative Potential of DPSCs and Revascularization: Direct, Paracrine or Autocrine Effect? Stem Cell Rev and Rep **17**: 1635-1646. DOI: 10.1007/s12015-021-10162-6.

Mosala Nezhad Z, Poncelet A, de Kerchove L, Gianello P, Fervaille C, El Khoury G (2016) Small intestinal submucosa extracellular matrix (CorMatrix®) in cardiovascular surgery: a systematic review. Interact Cardiovasc Thorac Surg **22**: 839-850. DOI: 10.1093/icvts/ivw020.

Murphy CM, Haugh MG, O'Brien FJ (2010) The effect of mean pore size on cell attachment, proliferation and migration in collagen-glycosaminoglycan scaffolds for bone tissue

engineering. Biomaterials **31**: 461-466. DOI: 10.1016/j.biomaterials.2009.09.063.

Nowwarote N, Petit S, Ferre FC, Dingli F, Laigle V, Loew D, Osathanon T, Fournier BPJ (2022) Extracellular Matrix Derived From Dental Pulp Stem Cells Promotes Mineralization. Front Bioeng Biotechnol **9**: 740712. DOI: 10.3389/fbioe.2021.740712.

Pineda JR, Polo Y, Pardo-Rodríguez B, Luzuriaga J, Uribe-Etxebarria V, García-Gallastegui P, Sarasua JR, Larrañaga A, Ibarretxe G (2022) Chapter 10 - In vitro preparation of human Dental Pulp Stem Cell grafts with biodegradable polymer scaffolds for nerve tissue engineering. In Methods in Cell Biology, ed. Ilio Vitale, Gwenola Manic, Lorenzo Galluzzi, **170**: 147-167. Academic Press, January 1. Methods in Stem Cell Biology - Part A. DOI: 10.1016/bs.mcb.2022.02.012.

Pisciotta A, Riccio M, Carnevale G, Beretti F, Gibellini L, Maraldi T, Cavallini GM, Ferrari A, Bruzzesi G, De Pol A (2012) Human serum promotes osteogenic differentiation of human dental pulp stem cells in vitro and in vivo. PLoS One **7**: e50542. DOI: 10.1371/journal.pone.0050542.

Rana D, Zreiqat H, Benkirane-Jessel N, Ramakrishna S, Ramalingam M (2017) Development of decellularized scaffolds for stem cell-driven tissue engineering. J Tissue Eng Regen Med **11**: 942-965. DOI: 10.1002/term.2061.

Rao Y, Zhu C, Suen HC, Huang S, Liao J, Ker DFE, Tuan RS, Wang D (2022) Tenogenic induction of human adipose-derived stem cells by soluble tendon extracellular matrix: composition and transcriptomic analyses. Stem Cell Res Ther **13**: 380. DOI: 10.1186/s13287-022-03038-0.

Rico-Llanos GA, Borrego-González S, Moncayo-Donoso M, Becerra J, Visser R (2021) Collagen Type I Biomaterials as Scaffolds for Bone Tissue Engineering. Polymers (Basel) **13**: 599. DOI: 10.3390/polym13040599.

Salgado AJ, Coutinho OP, Reis RL (2004) Bone tissue engineering: state of the art and future trends. Macromol Biosci **4**: 743-765. DOI: 10.1002/mabi.200400026.

Screen HRC, Berk DE, Kadler KE, Ramirez F, Young MF (2015) Tendon Functional Extracellular Matrix. J Orthop Res **33**: 793-799. DOI: 10.1002/jor.22818.

Sing KSW (1985) Reporting physisorption data for gas/solid systems with special reference to the determination of surface area and porosity (Recommendations 1984). Pure Appl Chem **57**: 603-619. DOI: 10.1351/pac198557040603.

Steward AJ, Kelly DJ (2015) Mechanical regulation of mesenchymal stem cell differentiation. J Anat **227**: 717-731. DOI: 10.1111/joa.12243.

Tirino V, Paino F, d'Aquino R, Desiderio V, De Rosa A, Papaccio G (2011) Methods for the identification, characterization and banking of human DPSCs: current strategies and perspectives. Stem Cell Rev Rep **7**: 608-615. DOI: 10.1007/s12015-011-9235-9.

Uribe-Etxebarria V, Luzuriaga J, García-Gallastegui P, Agliano A, Unda F, Ibarretxe G (2017) Notch/Wnt cross-signalling regulates stemness of dental pulp stem cells through expression of neural crest and core pluripotency factors. Eur Cell Mater **34**: 249-270. DOI: 10.22203/eCM.v034a16.

Xu J, Sun M, Tan Y, Wang H, Wang H, Li P, Xu Z, Xia Y, Li L, Li Y (2017) Effect of matrix stiffness on the proliferation and differentiation of umbilical cord mesenchymal stem cells. Differentiation **96**: 30-39. DOI: 10.1016/j.diff.2017.07.001.

Yang JZ, Qiu LH, Xiong SH, Dang JL, Rong XK, Hou MM, Wang K, Yu Z, Yi CG (2020) Decellularized adipose matrix provides an inductive microenvironment for stem cells in tissue regeneration. World J Stem Cells **12**: 585-603. DOI: 10.4252/wjsc.v12.i7.585.

Zhang YS, Yue K, Aleman J, Mollazadeh-Moghaddam K, Bakht SM, Yang J, Jia W, Dell'Erba V, Assawes P, Shin SR, Dokmeci MR, Oklu R, Khademhosseini A (2017) 3D Bioprinting for Tissue and Organ Fabrication. Ann Biomed Eng **45**: 148-163. DOI: 10.1007/s10439-016-1612-8.

Editor's note: The Scientific Editor responsible for this paper was Thimios Mitsiadis.